Multiscale modeling for food drying: A Downscaling approach

Zachary G. Welsh[a], Vindya Thathsaranee Weligama Thuppahige[a,b] and M. A. Karim*[a]

[a] Mechanical, Medical and Process Engineering, Queensland University of Technology, Brisbane, Australia

[b] Department of Food Science and Technology, Faculty of Agriculture, University of Ruhuna, Mapalana, Kamburupitiya, 81100, Sri Lanka

Corresponding author: Azharul Karim, Queensland University of Technology

2 George Street, QLD 4000 Australia, azharul.karim@qut.edu.au

ABSTRACT

Modeling the cellular level transport of plant-based food materials during drying is very complex. The transportation of intracellular water (ICW) significantly influences the drying kinetics; however, it is rarely considered in computational models. One approach which can investigate the impact of ICW on drying is multiscale modeling. However, most multiscale models fail to consider ICW or predetermine its trend and transport. This work aims to develop a multiscale downscaling model which can actively downscale a materials condition (dependent variables) to investigate the transport of ICW. Two different drying temperatures (47°C and 64°C) and the ICW transport at three different points of interest within the domain are investigated. The results were compared with experimental data and a control model. The downscaling model predicts drying at 47°C very well achieving mean relative errors (MREs) of 2.4% and 0.53% for the average moisture content and average temperature respectively. At 64°C, the model also predicts drying well achieving MREs of 5.32% and 0.78% for the average

moisture content and average temperature respectively. The ICW at each point of interest was calculated and its trend through the cell wall revealed interesting findings.

Keywords: multiscale modeling, cell rupturing, food drying, downscaling

1. INTRODUCTION

Plant-based food materials (PBFMs) have heterogeneous cellular structures comprising of three main cellular environments with each environment containing water of different characteristics: free water (FW) in intercellular spaces, intracellular water (ICW) in intracellular spaces and strongly bound water within the cell walls (Khan et al., 2018), Figure 1. Drying PBFMs involves simultaneous heat and multiphase mass transfer which dynamically changes a material in terms of its properties, characteristics and final quality (Weligama Thuppahige et al., 2024). These changes originate within the heterogeneous cellular structure of the material and propagate across multiple length scales (cellular/microscale to tissue/macroscale). These changes are a direct result of the complex internal water migration during drying, specifically the transport of ICW is a major concern during drying due to its influence on materials cellular structure. However, the transport of ICW is complex as it depends on the spatial and temporal drying conditions in addition to the property changes the material is experiencing (Welsh et al., 2023). ICW can transport two main ways, apoplastic transport where ICW migrates from intracellular spaces to intercellular spaces after a cell membrane ruptures or through symplastic transport where ICW migrates from cell to cell via fine capillaries (Weligama Thuppahige et al., 2024). The use of computational mathematical models to understand and control the effects of migrating ICW is essential in designing optimal drying processes. However, ICW and its effects are rarely considered in mathematical models of food drying.

[Figure 1 can be placed here]

Whitaker (1977) theory forms the foundation for many modern mathematical models. The theory derives a mechanistic macroscale model using the concept of a representative elementary volume (REV) considering the microscale heat, mass and momentum conservation equations of each phase (solid, liquid water, water vapor and air). However, Whitaker theory fails to consider the material's heterogeneity and assumes no ICW exists, rather it assumes all water is located outside the solid matrix. To overcome and compensate for this oversimplistic assumption, condition dependent properties are embedded within the computational models. Condition dependent properties are the properties which are accurate only when modeling the specific scenario/conditions in which the property was originally derived, for example properties which depend on a material's, drying conditions (i.e. air temperature, air speed) and/or the dryer configuration. Additionally, the further the simulated conditions deviate from the original conditions in which the property was derived, the less accurate the property becomes. One approach which can aid in transitioning away from condition-dependent properties while considering ICW is multiscale modeling. Multiscale modeling considers a series of sub-models over multiple length scales, giving it the ability to incorporate large amount of physics for a reasonable computational cost (Welsh et al., 2018). There are two main types of multiscale models, one way coupled models and two-way coupled (concurrent) models (Welsh et al., 2018). A one way coupled multiscale model transfers information in one direction, either through upscaling or downscaling. In such models, properties are often computed considering the structure of the particular material and upscaled to inform a larger scale. Alternatively, dependent variables can be downscaled to analyze the behavior at a smaller scale. Concurrent or two way coupled models, on the other hand, allow bidirectional information exchange. Here, data flows back and forth between scales, with each scale

evolving simultaneously and influencing the other. This concurrent exchange includes upscaling, downscaling, and mutual information exchange throughout the simulation, enabling both scales to adjust based on the other's evolving state (Welsh et al., 2018). Multiscale modeling has gained recent attention in the field of food drying modeling with various multiscale model being developed based on various assumptions. Qiu et al. (2022) developed a pore scale multiscale model for impingement drying of a porous slab. The work demonstrated the strength of predicting the drying performance through their multiscale approach to transport properties rather than the traditional condition dependent approach. Tan et al. (2023) also developed a pore-scale model for the heat-moisture and stress-stain distributions for high-moisture porous media. However, these works failed to consider ICW as all water considered was located in the pores/capillaries rather than the solid material.

Over the years there has been a few cellular models and multiscale models which have considered ICW within the solid material. Fanta et al. (2013) developed a microscale model to better understand the underlying phenomena of pear dehydrating under isothermal conditions at 25 ºC. The work considered water in each cellular environment, allowing the work to investigate the different pathways water can flow. The largest gradients in water content were observed across the cell walls and cell membranes. Rahman et al. (2018) also developed a micro-level transport model for drying apple parenchyma cells, considering ICW and conducted an in-depth sensitivity investigation. Prawiranto et al. (2018) constructed a cellular 3D continuum model for the dehydration of apple. The study considered water in various cellular environments and modelled dehydration with a predetermined set of cellular changes/conditions (Turgid, free shrinkage, lysis and plasmolysis). However, these works developed only cellular models rather than multiscale models, utilizing a single microscale domain to represent the transport occurring and often modelled predetermined conditions/scenarios for deformation and/or relative humidity. During drying, significant

spatial and temporal variations (in terms of moisture and temperature) develop within a product which cannot be fully understood/investigated with a singular microscale domain. These variations are especially evidence in the later stages of drying when the inner can be fully wet/saturated, whereas the outer cells of the material can be fully dried and deformed. Recently, Welsh et al. (2021a) developed a multiscale model for predicting the diffusivity of apple through upscaling during convective drying. The work considered ICW coupled with predetermined temperature dependent domains. The authors later extended their multiscale approach to inversely calculate the temporal cellular diffusivity of ICW in apples (Welsh et al., 2021b) and to construct a generalized diffusivity tensor which is applicable to multiple materials and conditions (Welsh et al., 2023). However, again their work focused on multiscale models which upscaled properties by utilizing predetermined microscale domains and/or considered every possible microscale scenario rather than predicting the spatiotemporal conditions occurring throughout the material. To predict the spatiotemporal conditions the cellular structure is experiencing a multiscale model which is capable of downscaling is required.

This work aims to develop a multiscale model capable of downscaling the dependent variables to appropriately predict the spatiotemporal conditions a material's cellular structure experiences during drying. The work investigates two different drying temperatures (47°C and 64°C) and focuses on the microscales at three different points of interest within the tissue domain. Additionally, the trend of ICW and its flux through the cell wall is investigated. The downscaling approach also incorporated cellular shrinkage through the shrinkage velocity approach paired with X-ray Micro-Computed Tomography (X-ray μCT) data to future improve the generalizability of the multiscale model. The modeling results are also compared to experimental data and a single scale control model.

2. Model Development

2.1 Drying model

A preliminary multiscale model was previously developed onsidering two spatial scales, a microscale and a macroscale (Welsh et al., 2021a), Figure 2. However, the previous model was only capable of upscaling information, specifically diffusivity, using predetermine conditions at the microscale. This study extends the preliminary model, allowing the model to downscale the required variables and evolve the microscale with time to investigate the different spatiotemporal conditions the cellular structure experiences throughout the entire material. Additionally, the ICW content required to calculate the diffusivity [Equation (16)], is calculate from the size of the intracellular space, outlined in 2.2.6, which is unique to this study. The modeling methods will present the multiscale governing equations, boundary conditions, properties, structure representation at each scale, computational approach, and temporal coupling. The modeling domains for both scales can be found in Figure 2. Additionally, the three points of interest, point 1 (P1), point 2 (P2) and point 3 (P3) are evenly distributed horizontally across the center of the macroscale [denoted by the red dots Figure 2 (a)].

[Figure 2 can be placed here]

2.2 Structure Representation at each scale

The macroscale can be considered as homogeneous following the common approach in literature, however, careful consideration needs to be taken when it comes to the microscale. Two common cellular structure definitions/classifications exist in the literature, (1) macroscopically connected and (2) disconnected inclusions, each effecting the model's assumptions and physics. Over the years, Perré (2019) has considered timber as connected inclusions for their multiscale models, resulting in an additional "secondary flux" of the

145 divergence of the microscopic flux being considered in the macroscale governing equations
146 when completing the scaling (Perré, 2007, 2019). Karunasena et al. (2015) considered the food
147 material as hexagon shaped cells evolving the porosity through removing some cells from the
148 arrangement for their meshfree models. The resulting structure appears to be disconnected
149 inclusions, though the work does not scale any results. Prawiranto et al. (2018) investigated the
150 transport and cellular changes of a single cuboctahedron shaped apple cell during drying. The
151 cell was located in the center of their 3D domain with voids (or pores) in all eight corners of
152 the cube, however, only basic volume averaging was considered to interpolate the results to the
153 macroscale. Fanta et al. (2014) and Rahman et al. (2018) considered an arrangement of multiple
154 intracellular and intercellular spaces while modeling the transport within the cellular structure
155 of PBFMs. The resulting structure is considered disconnected inclusions, though these works
156 also considered cell walls within the domains. Additionally, these works only model the
157 microscale transport phenomena and no scaling was conducted. In reality, fresh PBFMs
158 generally contain disconnected inclusions (pores) and during drying the structure evolves and
159 if cell rupturing occurs the inclusions will become connected. As a result, the model will
160 consider the structure as connected inclusions, however, as the model is being applied to
161 convective drying, internal convective flow can be neglected and the "secondary flux'
162 representing the flow through the cell structure is not considered. Nevertheless, if the multiscale
163 approach was applied to model other drying techniques (such as microwave drying) the
164 secondary flux would need to be considered.

165 The size of the microscale is important due to its effect on computational cost and
166 possible influence on the results. Additionally, the microscale must accurately represent the
167 dynamic microstructure, specifically the domain must represent the two key characteristics
168 which dynamically change during drying, namely the porosity and free/bound water.
169 Prawiranto et al. (2020) consider multiple domain sizes for dehydrating apple concluding

170 0.5mm cubed to be sufficient to accurately represent the structure. Carr et al. (2013) developed
171 a multiscale model for timber utilizing a microscale size of 50 μm with two sub-domains, a
172 cell and its cell wall. With this in mind, the microscale has a size of 250 μm with an initial cell
173 size of 215 μm calculated from the obtained X-ray μCT images, Figure 2.

174 *2.2.1 Macroscale conservation equations*

175 In an axisymmetric coordinate system, the macroscale transport model was developed
176 with the following assumptions: (1) internal convective flow and heat generation are negligible,
177 (2) drying air properties remain constant, (3) heating is axisymmetric, (4) moisture evaporates
178 solely from the surface, and (5) thermal equilibrium is maintained across all phases. The
179 macroscale mass and energy conservation equations are derived using Fick's law of diffusion
180 and Fourier's law of heat transfer. These equations determine the moisture concentration C
181 (mol/m³) and temperature T (K) as functions of position and time. The respective equations are
182 as follows (Golestani et al., 2013).

183 $$\frac{\partial C}{\partial t}+\frac{1}{r}\frac{\partial}{\partial r}\left[-D_{H,eff}\,r\,\frac{\partial C}{\partial r}\right]+\frac{\partial}{\partial z}\left[-D_{H,eff}\,\frac{\partial C}{\partial z}\right]=0\ , \tag{1}$$

184 $$\rho c_p\,\frac{\partial T}{\partial t}+\frac{1}{r}\frac{\partial}{\partial r}\left[-k\,r\,\frac{\partial T}{\partial r}\right]+\frac{\partial}{\partial z}\left[-k\,\frac{\partial T}{\partial z}\right]=0\ , \tag{2}$$

185 where t is the time (s), ρ represents the density of the food tissue (kg/m^3), c_p is the specific heat
186 of the food tissue (J/(kg·K)), k denotes the thermal conductivity of the food material (W/(m·K))
187 and $D_{H,eff}$ is the upscaled effective moisture diffusivity (m^2/s). The effective moisture diffusivity
188 varies with temperature and WC_{ICW}, the ICW content (%).

189 *2.2.2 Boundary conditions*

190 The macroscale boundary conditions for the mass flux and heat transfer at the exterior
191 surface was given by,

192 $$\mathbf{n}\cdot\left[-D_{H,eff}\nabla C\right]=h_m\frac{(p_{v\,eq}-p_{v\,air})}{RT}\,, \tag{3}$$

193 $$\mathbf{n}\cdot\left[-k\nabla T\right]=h_T(T-T_{air})-h_m\frac{(p_{v\,eq}-p_{v\,air})}{RT}h_{fg}M_w\,, \tag{4}$$

194 where h_m is the mass transfer coefficient (m/s), h_T is the heat transfer coefficient (W/(m^2·K)),
195 $p_{v\,eq}$ is the equilibrium vapor pressure, $p_{v\,air}$ is the vapor air pressure of ambient air (Pa) , **n** is
196 the unit vector normal to the boundary, R is the universal gas constant (J/(mol·K)), T_{air} is the
197 drying air temperature (K), M_w molar mass of water (g/mol) and h_{fg} is the latent heat of
198 evaporation (J/kg). The equilibrium vapor pressure for apple can be determined from the
199 sorption isotherm. Thus, the equilibrium vapor pressure for apple ($p_{v\,eq,apl}$) is (Ratti et al., 1989),

200 $$p_{v\,eq,apl}=p_{v\,sat}(T)\exp(-0.182M_{db}^{-0.696}+0.232e^{-43.949M_{db}}M_{db}^{0.0411}\ln\left[p_{v\,sat}(T)\right])\,. \tag{5}$$

201 The saturated vapor pressure is given by (Vega-Mercado et al., 2001),

202 $$p_{v\,sat}=\exp\left[-\frac{5800.2206}{T}+1.3915-0.0486T+0.4176\times10^{-4}T^2-0.1445\times10^{-7}T^3+6.546\ln(T)\right]. \tag{6}$$

203 The last boundary condition for the macroscale is the symmetric condition applied at
204 r=0, defined as

205 $$\mathbf{n}\cdot\left[-D_{H,eff}\nabla C\right]=0\,, \tag{7}$$

206 $$\mathbf{n}\cdot\left[-k\nabla T\right]=0\,. \tag{8}$$

207 *2.2.3 Microscale mass conservation*

208 To develop the multiscale model, a microscale was defined at each point within the
209 macroscale to represent the heterogeneous structure of the food. This approach is valid when
210 the scale parameter approaches zero, causing the heterogeneities to vanish and resulting in a

211 homogeneous material (Pavliotis & Stuart, 2008; Welsh et al., 2021a). This assumption is
212 crucial for deriving a model through homogenization and is often referred to as the separation
213 of scales (Auriault et al., 2010; Carr & Turner, 2014). The microscale considered two sub-
214 domains, ICW denoted as ω_{ICW} and intercellular water [free water (FW)] denote as ω_{FW}, Figure
215 2 (b). The macroscale mass transport, Equation (1), is coupled to the microscale mass transport
216 equation defined as,

217 $$\frac{\partial c}{\partial t}+\frac{\partial}{\partial x}\left(-D\frac{\partial c}{\partial x}\right)+\frac{\partial}{\partial y}\left(-D\frac{\partial c}{\partial y}\right)=0\ , \tag{9}$$

218 where c is the microscale concentration (mol/m^3) and D is the cellular diffusivity (m^2/s)
219 equaling D_{ICW} if x,y ϵ ω_{ICW} and D_{FW} if x,y ϵ ω_{FW}.

220

221 *2.2.4 Microscale boundary conditions*

222 The coupling between the macroscale and microscale variables occurs at the boundary
223 of the microscale given by,

224 $$c_{micro}(a,y)=c_{micro}(0,y)+a\frac{\partial C_{\psi}}{\partial r},\qquad 0<y<b \tag{10}$$

225 $$c_{micro}(x,b)=c_{micro}(x,0)+b\frac{\partial C_{\psi}}{\partial z},\qquad 0<x<a \tag{11}$$

226 where a and b are the size of the microscale domain and ψ is the point of interest. The fluxes
227 at the boundaries are also coupled through,

228 $$\begin{aligned} q_c(0,y)\cdot\mathbf{n}&=q_c(a,y)\cdot\mathbf{n}, \qquad 0<y<b\\ q_c(x,o)\cdot\mathbf{n}&=q_c(x,b)\cdot\mathbf{n}. \qquad 0<x<a \end{aligned} \tag{12}$$

229 The boundary condition for the cell wall is

$$\mathbf{n}\cdot\left[-D_{H,eff}\nabla C\right]=P_m(c-C), \tag{13}$$

where P_m is the permeability of the cell wall. The permeability of the cell wall does have some uncertainty as the thickness of the cell wall changes during drying (Joardder et al., 2015) and as such is investigated in a sensitivity investigation.

2.2.5 Macroscale and microscale diffusivity

To complete the multiscale model the diffusivity for the macroscale and cellular subdomains is required. The ICW diffusivity is (Welsh et al., 2021b),

$$D_{ICW}=\exp\left[-110.32+0.55536T_{cell}+0.095148WC_{ICW}-0.00090738T_{cell}^2-0.0007235WC_{ICW}^2\right], \tag{14}$$

where T_{cell} is the cell temperature (K) and WC_{ICW} is the intracellular water content (mass %). The diffusivity of FW is (Pace, 1962),

$$D_{FW}=2.26\times10^{-5}\left[\frac{T}{273.15}\right]^{1.81}. \tag{15}$$

The model does not actively upscale the cellular properties to form the macroscale diffusivity, rather the previously developed homogenized diffusivity is utilized (Welsh et al., 2021a). The function for the macroscale diffusivity is (Welsh et al., 2023),

$$D_{H,eff}=\exp\left[-106.6+0.5548T_{cell}+0.029502WC_{ICW}-0.00090648T_{cell}^2-0.00041019WC_{ICW}^2\right]. \tag{16}$$

2.2.6 Evolution of intracellular water- rupturing threshold

The ICW diffusivity function [Equation (14)] incorporates all three transport mechanisms (Welsh et al., 2023), therefore, cell rupturing must be incorporated within the evolution of the ICW. Welsh et al. (2023) introduced a rupturing threshold, exploiting the

macroscale equilibrium vapor pressure to determine if and when cell rupturing occurs within the material. Once the average macroscale equilibrium vapor pressure of the domain reaches the threshold, cells will begin to rupture. However, once the threshold was reached, Welsh et al. (2023) work utilized time dependent functions for ICW which require sophisticated microscale experimental techniques (such as nuclear magnetic resonance). This significantly limits the approaches applicability to other studies as these techniques are costly and not commonly available. As the current multiscale downscaling model includes an evolving microscale, the evolution of ICW can now be determined directly from the microscale. Therefore, when the cell is at its full size (215μm), the material is at its maximum ICW water content, 87.8% for apple (Khan et al., 2016). Once the cell rupturing threshold is reached the ICW is determined considering the change in cell size. The threshold of apple is considered as 7080 Pa for apple (Welsh et al., 2023).

2.2.7 Intracellular deformation

A shrinkage velocity approach was utilized to approximate the shrinkage of the intracellular space given by (Tuly et al., 2023),

$$\frac{\partial X}{\partial t} \cdot \mathbf{n} = v_n \ , \tag{17}$$

where v_n is the shrinkage velocity.

2.2.8 Other input parameters

The remaining input parameters are presented in Table 1.

[Table 1 can be placed here]

2.3 Simulation Methodology

The simulation procedure is outlined in Figure 3. The multiscale mathematical model was solved in LiveLink for MATLAB, a software package which combines COMSOL Multiphysics Simulations with MATLAB programming. Once the macroscale and microscale domains, governing equations, boundary conditions, properties and input parameters were defined, the model could be run from a MATLAB script file. To solve the multiscale model, the macroscale was first simulated for a single timestep, and the macroscale results were extracted. Then the required data was downscaled to the microscale and the microscale was simulated over its own timestep. Later, the extracted macroscale data was imported for the next timestep, and the procedure is repeated until the drying is complete. Lastly, a sensitivity investigation was conducted.

[Figure 3 can be placed here]

2.3.1 Macro-micro temporal coupling

The temporal coupling is extremely important to consider in a multiscale model and various approaches for temporal coupling exist (Welsh et al., 2018). The current model utilizes a Multigrid/heterogeneous multiscale method (HMM) approach, as shown in Figure 4, where the microscale is not continuously simulated. Microscale simulation was conducted as different timesteps (Figure 3) and key data is downscaled at the exchange timesteps. The downscaling model has a macroscale timestep of 60 seconds, a micro timestep of 0.1 seconds and an exchange timestep of 600 seconds. Additionally, the macroscale is simulated for 21600 seconds and 23400 seconds for drying at 47°C and 64°C respectively and the microscale is simulated for 5 seconds after each exchange step.

[Figure 4 can be placed here]

2.4 Experimental Investigations

Two separate experimental investigations were conducted, the macroscale drying experiments and X-ray μCT. The macroscale drying experiments were conducted to produce validation data to validate the output from the multiscale model whereas the X-ray μCT was conducted to investigate the evolution of the material's microstructure.

2.4.1 Macroscale drying experiments

Granny Smith apples at commercial maturity were purchased from a local supermarket and prepared following the standard sample preparation procedure (Asabe & Home). The samples were washed and then cut into cylindrical shapes using a stainless-steel Cork Borer (JH-1225). Each sample consisted of the mesocarp (pulp) portion, initially measuring 30 mm in length and 18 mm in diameter. Convective drying was performed at two selected temperatures within the typical air temperature range for drying (40–80 ºC): 47 ºC and 64 ºC, representing different levels of cellular deformation and ICW transport mechanisms. The dryer maintained an air velocity of 1 m/s and the airflow was perpendicular to the sample. Model validation was conducted using two data sets: average moisture content and average surface temperature of the samples. To measure moisture content, each sample was weighed individually at regular intervals. This occurred every 10 minutes during the first hour, then every 30 minutes until the drying process was completed. The samples were weighed using a digital balance with a 50 g capacity and ±0.001 g accuracy, with measurements completed within 10 seconds. A FLIR-E6390 thermal imaging camera was used to record surface temperature. This experimental procedure was repeated three times. The detailed drying experimental procedure and some of the results can be found in the authors' previous publication (Welsh et al., 2023).

2.4.2 X-ray μCT Experiment

In order to extract the cellular deformation of dried apple cells, both the fresh and convective dried (both at 45 °C and 60 °C) cylindrical-shaped Granny Smith apple samples were scanned using an X-ray μCT scanner (μCT50, Scanco Medical, Switzerland). Apple samples were packed in foam and horizontally placed in scanning tubes with a diameter of 34mm. The native resolution, electric potential, current and the power used for these scans were as 10.3 μm^3, 55 kvp, 145 μA, and 8 W, respectively with an average sample scanning time of 1000 ms and an Aluminum filter (0.1 mm). The scans were carried out in triplicates. Once the scans were completed, the image stacks were exported as DIACOM files into Mimics (Version 24.0, Materialise NV, Belgium) for segmentation using semi-automated thresholding. The consistency of the segmentations was ensured by maintaining a constant threshold value. It should be noted due to the study requirements and equipment limitations the X-ray μCT experimentation was conducted on cylindrical samples with a height of 15 mm and a diameter of 8mm 15 mm and a diameter of 8mm drying at an average temperature of 45°C and 60°C.

3. Results

The results are presented into five main sections, the cellular deformation, the macroscale drying kinetics, the macroscale temperature evolution, the ICW results and a sensitivity investigation. Three points of interest within the macroscale domain, (P1, P2 and P3) were selected along the center of the domain to analyses the model and approach, visually shown in Figure 2. These points were selected as examples to demonstrate how the microscales vary spatially depending on its location in the macroscale. The multiscale downscaling model was compared to the experimental data and the single scale macroscale model as a control (Welsh et al., 2023). All properties and heat and mass transfer coefficients were the same for the control and downscaling model.

346 *3.1 Cellular deformation*

347 X-ray μCT was utilized to extract the cellular deformation information of granny smith
348 apple dried at 45°C and 60°C. Evaluating 30 intracellular spaces resulted in averages sizes of
349 215.4 ± 30 μm to fresh apples cells, 128.15 ± 10 μm for dried apple cells with convective air
350 at 45°C to 0.8 kg/kg dry bases and 119.10 ± 10 μm for dried apple cells with convective air at
351 60°C to 1.23 kg/kg dry bases, Figure 5. This resulted in, using Equation (17), temperature
352 dependent shrinkage velocities of $-25x10^{-9}$ m/s and $-30x10^{-9}$ m/s for drying at 47°C and apple
353 dried 64°C respectively. It should be noted, the shrinkage velocity also had to consider the
354 multiscale temporal coupling.

355 **[Figure 5 can be placed here]**

356

357

358 *3.2 Macroscale - Drying Kinetics*

359 The downscaling model accurately predicted the moisture transport at 47°C achieving a mean
360 relative error (MRE) of 2.4% when compared to the experimental results (Welsh et al., 2023),
361 Figure 6. The control model (Welsh et al., 2023) achieved a similarly low MRE of 1.52%. The
362 multiscale downscaling model slightly overpredicts the experimental data consistently till the
363 later stages of drying. In the later stage, the model slightly underpredicts the transport matching
364 the trend of the control model. The downscaling model and control model resulted in almost
365 identical diffusivities between 1.94×10^{-10} and 2.16×10^{-10} m^2/s for drying at 47°C, Figure 7. At
366 64°C the downscaling model predicted the moisture transport accurately achieving a MRE of
367 5.32% when compared to the experimental results, Figure 6. The control macroscale model
368 achieved a similarly low MRE of 4.80%, predicting the experimental data slightly better. The
369 multiscale downscaling model slightly overpredicted the experimental data between 30-180

mins for drying at 64°C and then slightly underpredicted the experimental data in the later stages. The lack of macroscale deformation is likely contributing to the difference in the later stages of drying. When drying at 64°C, the rupture threshold is reached and the downscaling model estimated the ICW content from the change in cell size. This resulted in a diffusivity range of 4.78×10^{-10} – 2.58×10^{-10} m^2/s which is similar to the control model, Figure 7. The resulting diffusivities fell in the typically range of 10^{-11} and 10^{-9} m^2/s for food material (Panagiotou et al., 2004; Saravacos & Maroulis, 2001).

[Figure 6 can be placed here]

[Figure 7 can be placed here]

3.3 Macroscale – Temperature evolution

The downscaling model accurately predicted the average sample temperature for drying at both 47°C and 64°C, with MREs of 0.53% and 0.78% respectively, Figure 8. Similarly, the control model achieved MREs of 0.46% and 0.89% respectively when compared to the experimental results, Figure 8. There is minimal difference between the downscaling model and the control model at both drying temperatures. This is because no properties within the heat transfer are in terms of ICW, rather just macroscale moisture. However, both the multiscale downscaling model and the control model significantly overpredicted the experimental data in the early stages of drying. It should be noted, the experimental data is of a sample under convective drying with perpendicular airflow. Due to the perpendicular airflow, a large 'dead zone' existed behind the trailing edge of the sample during drying and thus, the heat transfer coefficient heavily effected in this region of the sample (Khan et al., 2020). As a result, the temporally and spatially constant heat transfer coefficient contributed heavily to the initial overprediction.

[Figure 8 can be placed here]

3.4 Intracellular water transport

The spatial moisture profile at macroscale and the three locations of interest for drying at 47°C and 64°C can be seen in Figure 9 and Figure 10 respectively, in which the dashed circle denotes the original cell size. It should be noted, the moisture profile shown in Figure 9 and Figure 10 are at the exchange steps. As expected, each point of interest has its own temporal moisture profile corresponding to the macroscale conditions occurring at that particular point. This is unlike the existing microscale models in literature which utilize a single domain to characterize the sample transport (Rahman et al., 2018). As the moisture profile develops within the sample, the intracellular space at the outside point (P3), dries first. As expected, in the later stages, the intracellular space at P3 is entirely dry whereas the intracellular space at P1 only starts to dry. This trend observed in both drying temperatures. Additionally, due to the temporal coupling and the size of the exchange time step utilized, there can be a delay in the moisture transfer between the end of the microscale and the initialization of the microscale. The microscale is only simulated for 5 seconds after an exchange step and the data exchange only occurs every 600 seconds (10 mins). This creates a time skip of 595 seconds. Evidence of this delay can be seen in the microscale at P3 at 100 minutes in Figure 9.

[Figure 9 can be placed here]

[Figure 10 can be placed here]

The average moisture content of the intracellular spaces at each point of interest and the flux through the cell walls can be found in Figure 11 (a) and (b) respectively. Throughout drying, the flux through the cell wall at P3 (point closest to the exterior wall) is significantly

larger than the flux at P2 and P1, especially in the middle portion of drying. This trend is consistent for both drying temperatures. Additionally, the flux through the cell walls at each point exhibit peaks at different stages of drying and as expected drying at higher temperatures resulted in additional flux through the cell wall. P3 near the outside wall peaks first at 110 mins for drying at 64°C with a magnitude of -4.33×10^{-7} mol/s. For drying at 47°C, P3's peak occurs later at 170 mins. The different shrinkage velocity for the two drying temperatures resulted in slightly different final cell sizes of 119 μm for drying at 47°C and 109 μm for 64°C following the trend uncovered in the X-ray μCT investigation. It should be noted, the shrinkage velocity approach results in ideal shrinkage.

[Figure 11 can be placed here]

3.5 Sensitivity Investigation

A sensitivity analysis was conducted on a parameter with uncertainty, specifically on cell wall permeability, which was considered constant. Literature has demonstrate when drying at 70°C the average cell wall thickness of granny smith apples changes from 9.312μm when fresh to 4.685μm when dried (Joardder et al., 2015). This change mainly occurs when the FW content reduces surrounding an intracellular space and ICW begins to transport through the cell wall. Permeability is the diffusivity of a cell wall over its width, hence as diffusivity and the wall thickness changes uncertainty exists within permeability. To evaluate the sensitivity of the downscaling model, the cell permeability was investigated by varying the utilized value by ±10% while drying at 47°C. This parameter was investigated in relation to the average macroscale moisture content (kg/kg dry bases), the microscale concentrations (mol) and the cell wall flux (mol/s).

The downscaling model's sensitivity to cell wall permeability can be seen in Figure 12. The macroscale moisture content and the microscale ICW content were not sensitive to the change in cell wall permeability with their magnitudes and trend not changing. However, as permeability is key in the cellular boundary condition, the changes in permeability do influence the magnitude of the cell wall flux. Plus 10% results in an increase to the magnitude of the flux whereas minus 10% decrease the flux through the cell wall. The difference is significant and clearly evidenced for P3 but much smaller for P1and P2.

[Figure 12 can be placed here]

4. Discussion

The downscaling model provides new insight into the transport of ICW while accurately predicting drying at 47°C and 64°C. When drying at lower temperatures (47°C) the consideration of a constant ICW with the upscaled diffusivity [Equation (16)] creates a fairly constant diffusivity which was sufficient to accurately predict drying. This finding is consistent with pre-existing literature (Defraeye & Verboven, 2017; Welsh et al., 2023). When drying at medium temperatures (64°C), the multiscale downscaling model accurately predicted drying, suggesting that ICW estimation based on cell size changes is suitable to utilize the upscaled diffusivity property with the rupture threshold. This technique enhances the generalizability of the modeling approach and differs from previously published work (Welsh et al., 2023). Notably, the shrinkage velocity approach, based on X-ray μCT data, was employed to estimate cell size changes. The model could be further refined by incorporating a physics-based approach to cellular deformation, such as van der Sman et al. (2024)'s recent work on pore development in viscoelastic foods during drying.

The microscales at the three points of interest provided interesting insight, Figure 9 to Figure 10. Each produced spatially dependent microscales which is different to the previously published microscale models where a single microscale is used to predict the material's evolution (Rahman et al., 2018). Specifically, the flux through the cell wall is very unique for each intracellular space at each point of interest. The microscale near the outside edge (P3) experienced significantly more flux throughout the entire duration of drying. The magnitude of the flux also depended on the drying air temperature and is sensitive to the magnitude of the cell wall permeability. Literature has demonstrated when drying at medium temperature (above 50°C), progressive and ultimate cell rupturing would have occurred (Khan et al., 2018). It is theorized, due to the convective heating profile, when the surface reaches 50°C the intracellular space near the surface lose their rigidity and tend to become droopy, hence nearing their rupturing limit (Khan et al., 2018). The intracellular spaces lose turgor pressure and tend to fail due to the imposed thermal stress of continuous penetration of heat energy. Though past research on cell rupturing has been conducted using nuclear magnetic resonance which is only able to produce results of the entire sample (domain averages) and does not give insight into the spatial propagation of the rupturing mechanism. Further investigation is needed in the future, but the cell wall flux may provide valuable insight in predicting when and/or where cell rupturing spatially propagates within PBFMs.

One key component of any multiscale model is its temporal coupling. Previous works within the field (Rahman et al., 2018) have only utilized multiscale modeling to upscale properties. Such an approach produces a property, often a homogenized property, through computing the microscale in a steady state condition for specific discrete points of interest (i.e. when a cell has a moisture content of 3 kg/kg dry bases). However, as the current study is a multiscale downscaling model, the microscale evolves with time and hence a temporal coupling is required. Specifically, the HMM approach was utilized. This approach saves on

computational cost but does not simulate the microscale for the entire simulation (as described in 2.3.1 Macro-micro temporal coupling). Instead, the approach just computes the microscale for a small period of time after the exchange point. Hence, there is a portion of time (9.16 mins) which is skipped in between the exchange steps. This saves on computational cost however it can create a delayed effect on the transport, which will not always be desired. Depending on the purpose of the model and the available computational resources, this skipped time can be either reduced or increased. Alternatively, temporal couplings like the continuous HMM simulate the microscale across the entire time period and can be employed based on the model's purpose.

5. Conclusion

The multiscale model accurately described the drying process at both low and medium temperatures (47°C and 64°C). For drying at 47°C the model achieved MREs of 2.4% and 0.53% for average macroscale moisture content and temperature respectively and for drying at 64°C the model achieved MREs of 5.32% and 0.78% for average macroscale moisture content and temperature, respectively. Furthermore, the integration of downscaling coupling in the model provided valuable insights into the microscale evolution during drying. When drying at medium temperatures, the rupturing threshold was reached and the ICW of the sample was predicted considering the changes in the cells size. To demonstrate the capacity of the approach, microscales at three points of interest were investigated. Each microscale evolved differently depending on the applied drying conditions and their spatial location within the domain. The ICW trend through the cell wall provided important insight into what the cell wall experiences at different locations and was also unique for each microscale location and drying temperature. Additionally, the convective drying temperature significantly influenced the magnitude of the

515 flux the cell wall experienced due to the moisture migration. Further investigating is required
516 but such a multiscale approach could be utilized to investigate how cell rupturing propagates
517 within a domain. The model could also be refined to calculate cellular deformation through a
518 more mathematical approach with deformation on both spatial scales coupled with some
519 consideration of cell rupturing. The multiscale downscaling approach, coupled with Welsh et
520 al. (2023) upscaling technique will facilitate the construct of an in-depth concurrent multiscale
521 model being developed in the future.

522 **Acknowledgements**

523 This research work is supported by Australian Research council (DP220103668). The
524 authors would like to acknowledge Dr. M.U.H Joardder for his suggestion in relation to the
525 cellular transport. Moreover, the authors also wish to express their gratitude to the KG-Q
526 Research Facility, QUT for allowing access to the X-ray μCT equipment.

527

6. References

Asabe, J., & Home, A. American society of agricultural and biological engineers.

Auriault, J.-L., Boutin, C., & Geindreau, C. (2010). *Homogenization of coupled phenomena in heterogenous media* (Vol. 149). John Wiley & Sons.

Białobrzewski, I. (2006). Simulation of changes in the density of an apple slab during drying. *International Communications in Heat and Mass Transfer*, *33*(7), 880-888. https://doi.org/https://doi.org/10.1016/j.icheatmasstransfer.2006.02.017

Carr, E. J., & Turner, I. W. (2014). Two-scale computational modelling of water flow in unsaturated soils containing irregular-shaped inclusions. *International Journal for Numerical Methods in Engineering*, *98*, 157-173. https://doi.org/https://doi.org/10.1002/nme.4625

Carr, E. J., Turner, I. W., & Perré, P. (2013). A dual-scale modeling approach for drying hygroscopic porous media. *Multiscale Modeling & Simulation*, *11*, 362-384. https://doi.org/10.1137/120873005

Cengel, Y. (2003). *Heat, Transfer Mass: A practical approach*. Mc-Graw Hill Education, Columbus, GA, USA.

Cengel, Y. A., & Boles, M. A. (2002). Thermodynamics: an engineering approach. *Sea*, *1000*, 8862.

Defraeye, T., & Verboven, P. (2017). Convective drying of fruit: Role and impact of moisture transport properties in modelling. *Journal of Food Engineering*, *193*, 95-107. https://doi.org/http://dx.doi.org/10.1016/j.jfoodeng.2016.08.013

Fanta, S. W., Abera, M. K., Aregawi, W. A., Ho, Q. T., Verboven, P., Carmeliet, J., & Nicolai, B. M. (2014). Microscale modeling of coupled water transport and mechanical deformation of fruit tissue during dehydration. *Journal of Food Engineering*, *124*, 86-96. https://doi.org/10.1016/j.jfoodeng.2013.10.007

Fanta, S. W., Abera, M. K., Ho, Q. T., Verboven, P., Carmeliet, J., & Nicolai, B. M. (2013). Microscale modeling of water transport in fruit tissue. *Journal of Food Engineering*, *118*, 229-237. https://doi.org/https://doi.org/10.1016/j.jfoodeng.2013.04.003

Ferrando, M., & Spiess, W. E. L. (2001). Cellular response of plant tissue during the osmotic treatment with sucrose, maltose, and trehalose solutions. *Journal of Food Engineering*, *49*(2), 115-127. https://doi.org/https://doi.org/10.1016/S0260-8774(00)00218-1

559 Golestani, R., Raisi, A., & Aroujalian, A. (2013). Mathematical modeling on air drying of
560 apples considering shrinkage and variable diffusion coefficient. *Drying Technology*,
561 *31*, 40-51. https://doi.org/https://doi.org/10.1080/07373937.2012.714826
562 Joardder, M. U., Brown, R. J., Kumar, C., & Karim, M. (2015). Effect of cell wall properties
563 on porosity and shrinkage of dried apple. *International Journal of Food Properties*,
564 *18*(10), 2327-2337. https://doi.org/https://doi.org/10.1080/10942912.2014.980945
565 Karunasena, H. C. P., Gu, Y. T., Brown, R. J., & Senadeera, W. (2015). Numerical
566 investigation of plant tissue porosity and its influence on cellular level shrinkage during
567 drying. *Biosystems Engineering*, *132*(Supplement C), 71-87.
568 https://doi.org/https://doi.org/10.1016/j.biosystemseng.2015.02.002
569 Khan, M. I. H., Farrell, T., Nagy, S. A., & Karim, M. A. (2018). Fundamental Understanding
570 of Cellular Water Transport Process in Bio-Food Material during Drying. *Scientific*
571 *Reports*, *8*(1), 15191. https://doi.org/https://doi.org/10.1038/s41598-018-33159-7
572 Khan, M. I. H., Wellard, R. M., Nagy, S. A., Joardder, M. U. H., & Karim, M. A. (2016).
573 Investigation of bound and free water in plant-based food material using NMR T2
574 relaxometry. *Innovative Food Science & Emerging Technologies*, *38*, 252-261.
575 https://doi.org/https://doi.org/10.1016/j.ifset.2016.10.015
576 Khan, M. Imran H., Welsh, Z., Gu, Y., Karim, M. A., & Bhandari, B. (2020). Modelling of
577 simultaneous heat and mass transfer considering the spatial distribution of air velocity
578 during intermittent microwave convective drying. *International Journal of Heat and*
579 *Mass Transfer*, *153*, 119668.
580 https://doi.org/https://doi.org/10.1016/j.ijheatmasstransfer.2020.119668
581 Mattea, M., Urbicain, M. J., & Rotstein, E. (1986). Prediction of Thermal Conductivity of
582 Vegetable Foods by the Effective Medium Theory. *Journal of Food Science*, *51*(1),
583 113-115. https://doi.org/https://doi.org/10.1111/j.1365-2621.1986.tb10848.x
584 Mavroudis, N. E., Gekas, V., & Sjöholm, I. (1998). Osmotic dehydration of apples—effects of
585 agitation and raw material characteristics. *Journal of Food Engineering*, *35*(2), 191-
586 209. https://doi.org/https://doi.org/10.1016/S0260-8774(98)00015-6
587 Moshelion, M., Moran, N., & Chaumont, F. (2004). Dynamic changes in the osmotic water
588 permeability of protoplast plasma membrane. *Plant Physiol*, *135*(4), 2301-2317.
589 https://doi.org/https://doi.org/10.1104/pp.104.043000
590 Pace, E. L. (1962). Scientific foundations of vacuum technique (Dushman, Saul). *Journal of*
591 *Chemical Education*, *39*(8), A606. https://doi.org/https://doi.org/10.1021/ed039pA606

592 Panagiotou, N., Krokida, M., Maroulis, Z., & Saravacos, G. (2004). Moisture diffusivity:
593 literature data compilation for foodstuffs. *International Journal of Food Properties*,
594 *7*(2), 273-299. https://doi.org/https://doi.org/10.1081/JFP-120030038
595 Pavliotis, G. A., & Stuart, A. (2008). *Multiscale methods: averaging and homogenization*.
596 Springer Science & Business Media.
597 Perré, P. (2007). Multiscale aspects of heat and mass transfer during drying. *Transport in*
598 *Porous Media*, *66*, 59-76. https://doi.org/https://doi.org/10.1007/s11242-006-9022-2
599 Perré, P. (2019). Coupled heat and mass transfer in biosourced porous media without local
600 equilibrium: A macroscopic formulation tailored to computational simulation.
601 *International Journal of Heat and Mass Transfer*, *140*, 717-730.
602 https://doi.org/https://doi.org/10.1016/j.ijheatmasstransfer.2019.06.043
603 Prawiranto, K., Carmeliet, J., & Defraeye, T. (2020). Identifying in silico how microstructural
604 changes in cellular fruit affect the drying kinetics [10.1039/D0SM00749H]. *Soft*
605 *Matter*, *16*(43), 9929-9945. https://doi.org/10.1039/D0SM00749H
606 Prawiranto, K., Defraeye, T., Derome, D., Verboven, P., Nicolai, B., & Carmeliet, J. (2018).
607 New insights into the apple fruit dehydration process at the cellular scale by 3D
608 continuum modeling. *Journal of Food Engineering*, *239*, 52-63.
609 https://doi.org/https://doi.org/10.1016/j.jfoodeng.2018.06.023
610 Qiu, S., Xu, S., Rao, B., Mujumdar, A. S., & Xu, P. (2022). A multi-scale model for
611 impingement drying of porous slab. *Journal of Food Engineering*, *335*, 111194.
612 https://doi.org/https://doi.org/10.1016/j.jfoodeng.2022.111194
613 Rahman, M. M., Kumar, C., Joardder, M. U. H., & Karim, M. A. (2018). A micro-level
614 transport model for plant-based food materials during drying. *Chemical Engineering*
615 *Science*, *187*, 1-15. https://doi.org/10.1016/j.ces.2018.04.060
616 Ratti, C., Crapiste, G., & Rotstein, E. (1989). A new water sorption equilibrium expression for
617 solid foods based on thermodynamic considerations. *Journal of Food Science*, *54*(3),
618 738-742. https://doi.org/https://doi.org/10.1111/j.1365-2621.1989.tb04693.x
619 Saravacos, G. D., & Maroulis, Z. B. (2001). *Transport properties of foods*. CRC Press.
620 Tan, L., Yuan, Y., Zhao, Z., Xu, Y., & Yuan, Y. (2023). Insights in mechanism of drying
621 shrinkage by pore-scale modeling of heat-moisture and stress-strain distribution for
622 high-moisture porous media. *International Journal of Thermal Sciences*, *188*, 108226.
623 https://doi.org/https://doi.org/10.1016/j.ijthermalsci.2023.108226

624 Tuly, S. S., Joardder, M. U. H., Welsh, Z. G., & Karim, A. (2023). Mathematical Modelling of
625 Heat and Mass Transfer during Jackfruit Drying Considering Shrinkage. *Energies*,
626 *16*(11), 4461. https://www.mdpi.com/1996-1073/16/11/4461
627 van der Sman, R., Curatolo, M., & Teresi, L. (2024). Pore development in viscoelastic foods
628 during drying [10.1039/D4SM00201F]. *Soft Matter*, *20*(26), 5183-5194.
629 https://doi.org/10.1039/D4SM00201F
630 Vega-Mercado, H., Marcela Góngora-Nieto, M., & Barbosa-Cánovas, G. V. (2001). Advances
631 in dehydration of foods. *Journal of Food Engineering*, *49*(4), 271-289.
632 https://doi.org/https://doi.org/10.1016/S0260-8774(00)00224-7
633 Weligama Thuppahige, V. T., Welsh, Z. G., Joardder, M., & Karim, A. (2024). Recent
634 advances in determining the cellular-level property evolutions of plant-based food
635 materials during drying. *Trends in Food Science & Technology*, *143*, 104291.
636 https://doi.org/https://doi.org/10.1016/j.tifs.2023.104291
637 Welsh, Z., Simpson, M. J., Khan, M. I. H., & Karim, M. (2018). Multiscale Modeling for Food
638 Drying: State of the Art. *Comprehensive Reviews in Food Science and Food Safety*,
639 *17*(5), 1293-1308. https://doi.org/https://doi.org/10.1111/1541-4337.12380
640 Welsh, Z. G., Khan, M. I. H., & Karim, M. (2021a). Multiscale modeling for food drying: A
641 homogenized diffusion approach. *Journal of Food Engineering*, *292*, 110252.
642 https://doi.org/https://doi.org/10.1016/j.jfoodeng.2020.110252
643 Welsh, Z. G., Simpson, M. J., Khan, M. I. H., & Karim, A. (2021b). A multiscale approach to
644 estimate the cellular diffusivity during food drying. *Biosystems Engineering*, *212*, 273-
645 289. https://doi.org/https://doi.org/10.1016/j.biosystemseng.2021.10.017
646 Welsh, Z. G., Simpson, M. J., Khan, M. I. H., & Karim, M. A. (2023). Generalized moisture
647 diffusivity for food drying through multiscale modeling. *Journal of Food Engineering*,
648 *340*, 111309. https://doi.org/https://doi.org/10.1016/j.jfoodeng.2022.111309
649 Whitaker, S. (1977). Simultaneous Heat, Mass, and Momentum Transfer in Porous Media: A
650 Theory of Drying. *Advances in Heat Transfer*, *13*, 119-203.
651 https://doi.org/http://dx.doi.org/10.1016/S0065-2717(08)70223-5

652

653

654 **Figures:**

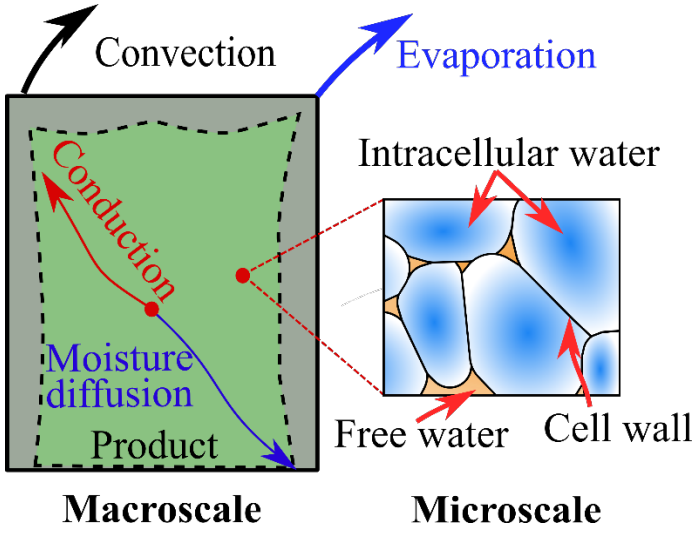

655

656 Figure 1. Cellular structure of plant-based food material

657

658

659

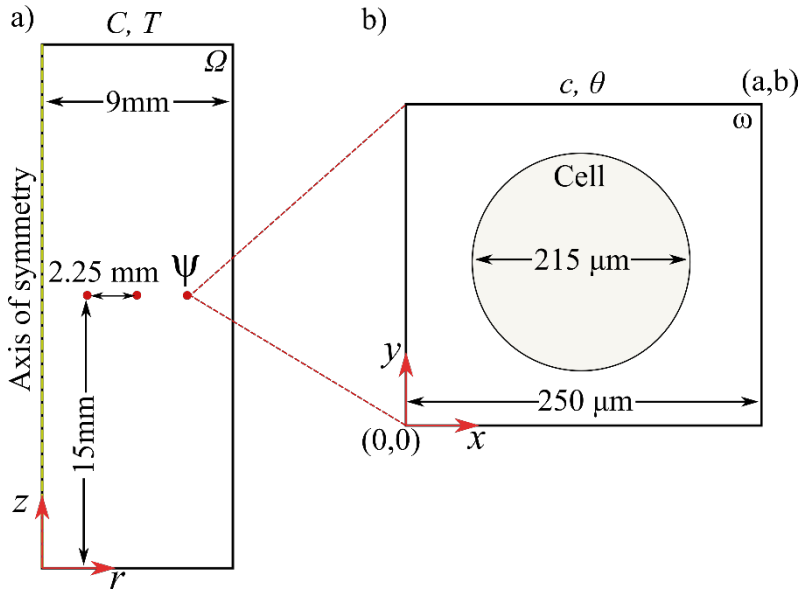

660

661 Figure 2. Domains, a) axisymmetric macroscale domain with the three locations of

662 interest marked by red dots, and b) microscale domain.

663

664

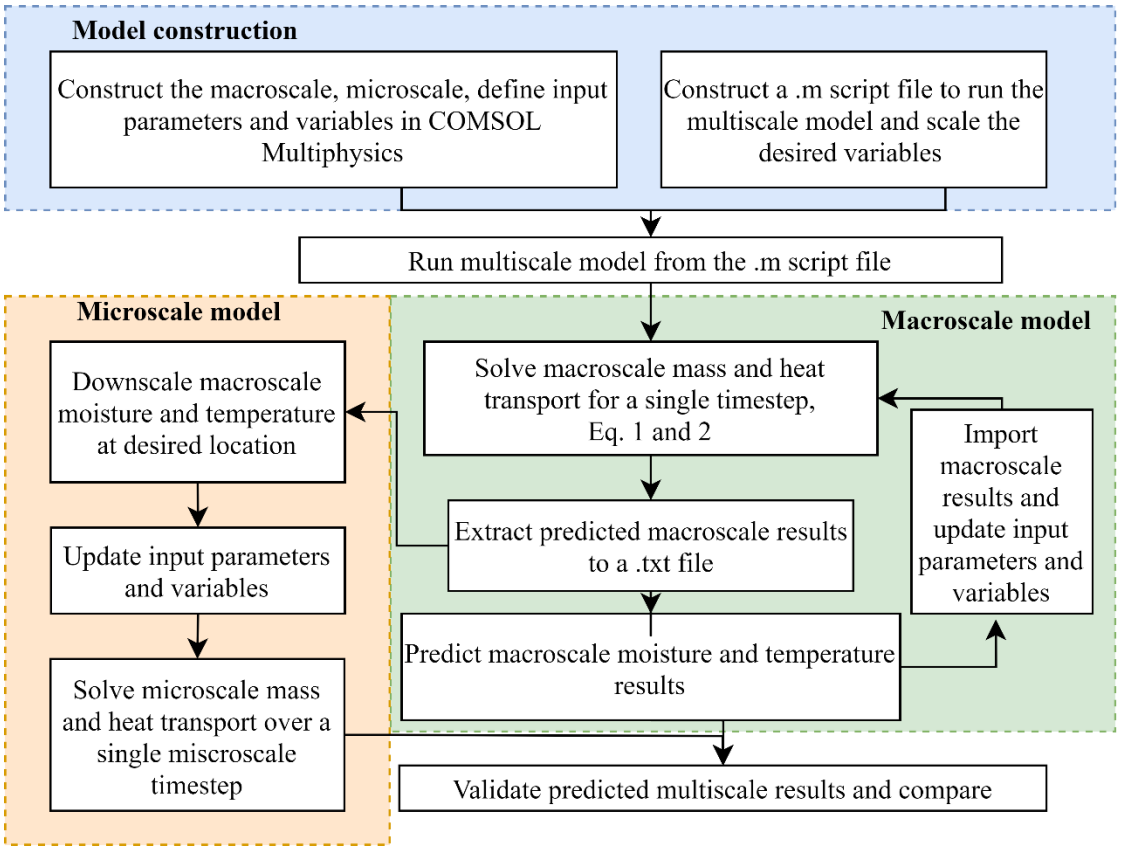

665

666 Figure 3. Simulation Methodology

667

668

669

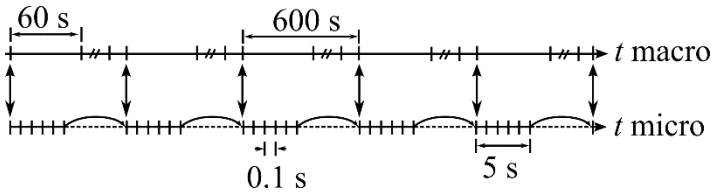

670

671 Figure 4. Multiscale temporal coupling.

672

673

674

a) b) c)

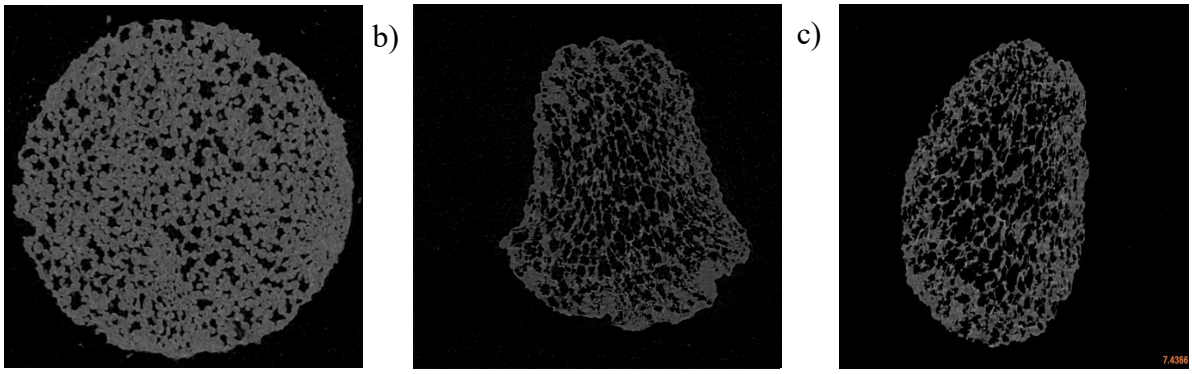

675

676 Figure 5. X-ray μCT images of, (a) fresh, (b) dried at 45°C at 0.8 kg/kg dry bases, (b)
677 dried at 60°C at 1.23 kg/kg dry bases.

678

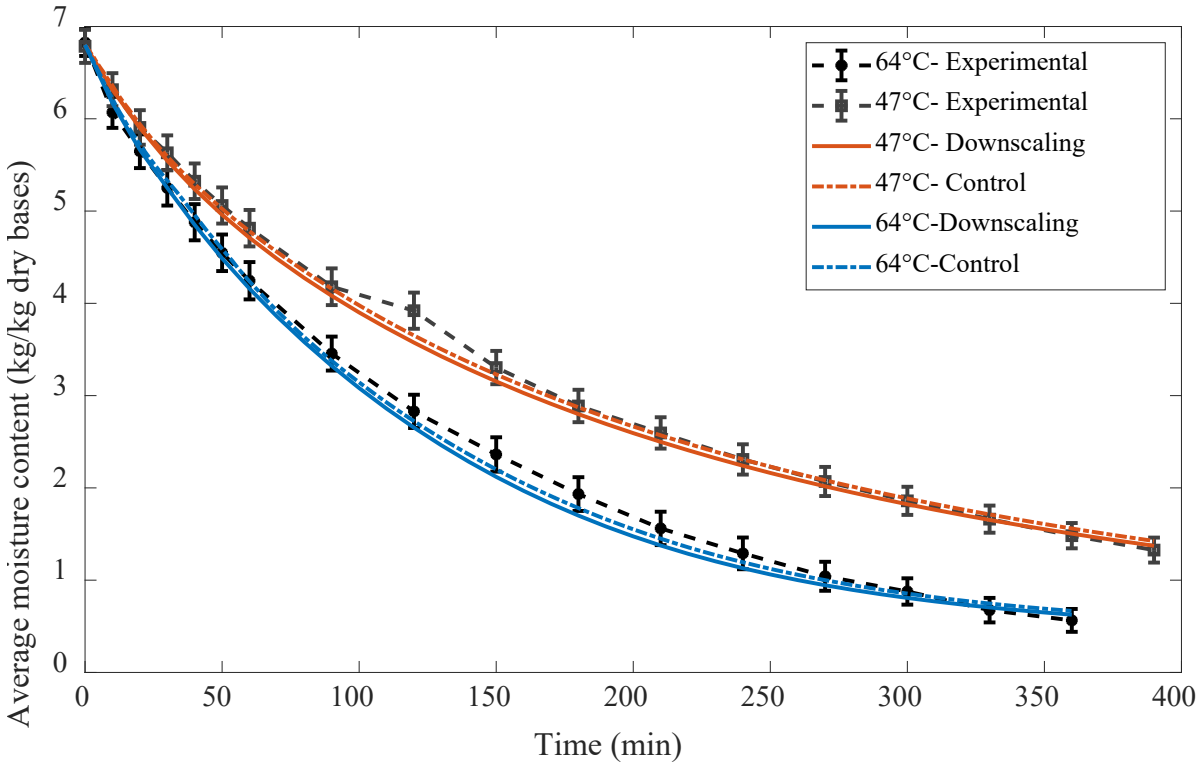

679

680 Figure 6. Average moisture content (kg/kg dry bases) at low and medium temperature

681 drying.

682

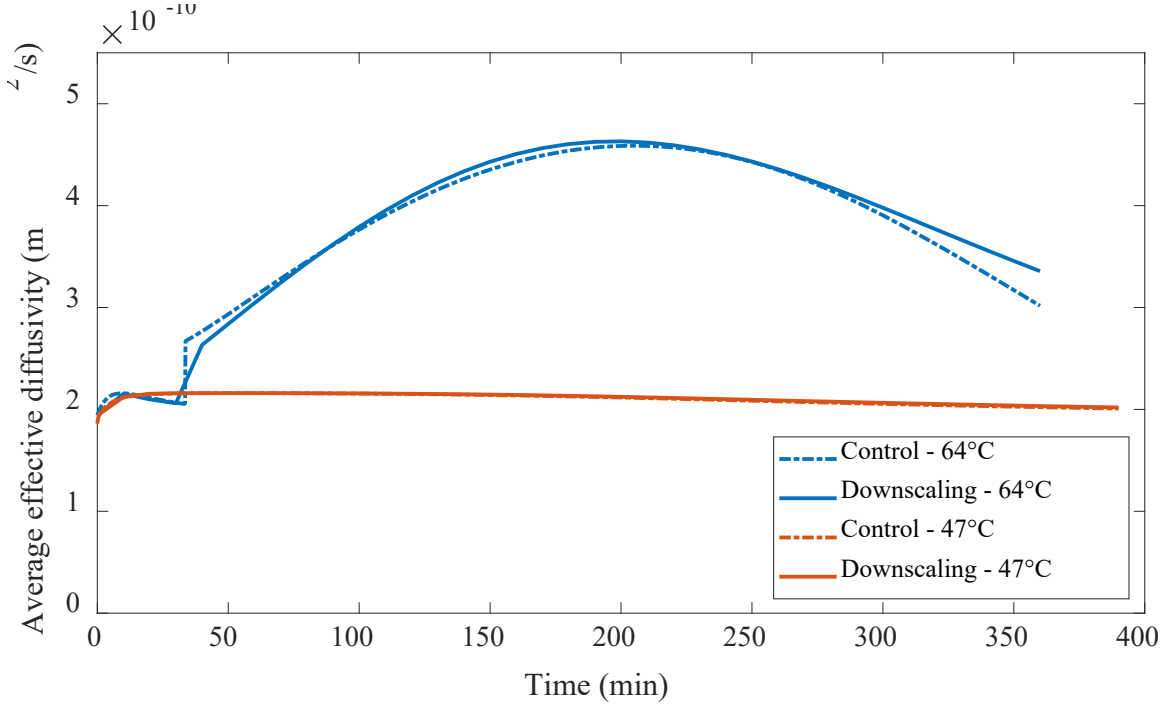

683

684 Figure 7. Average macroscale diffusivity (m^2/s) for both drying temperatures.

685

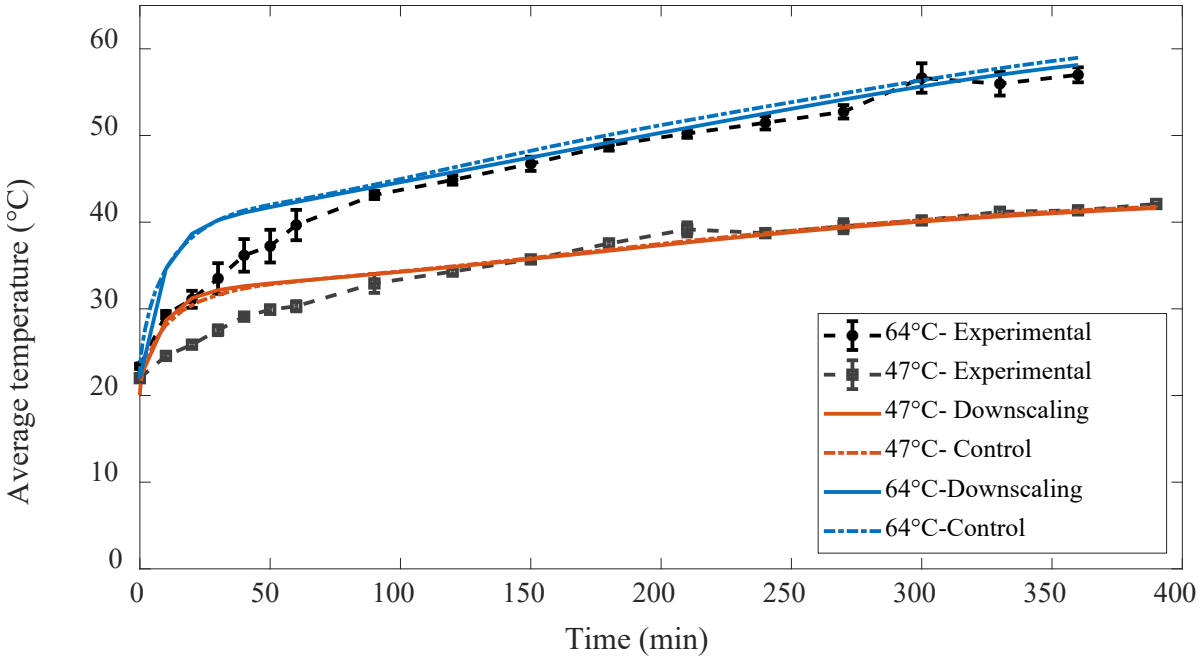

686

687 Figure 8. Average surface temperature (°C) for both drying temperatures.

688

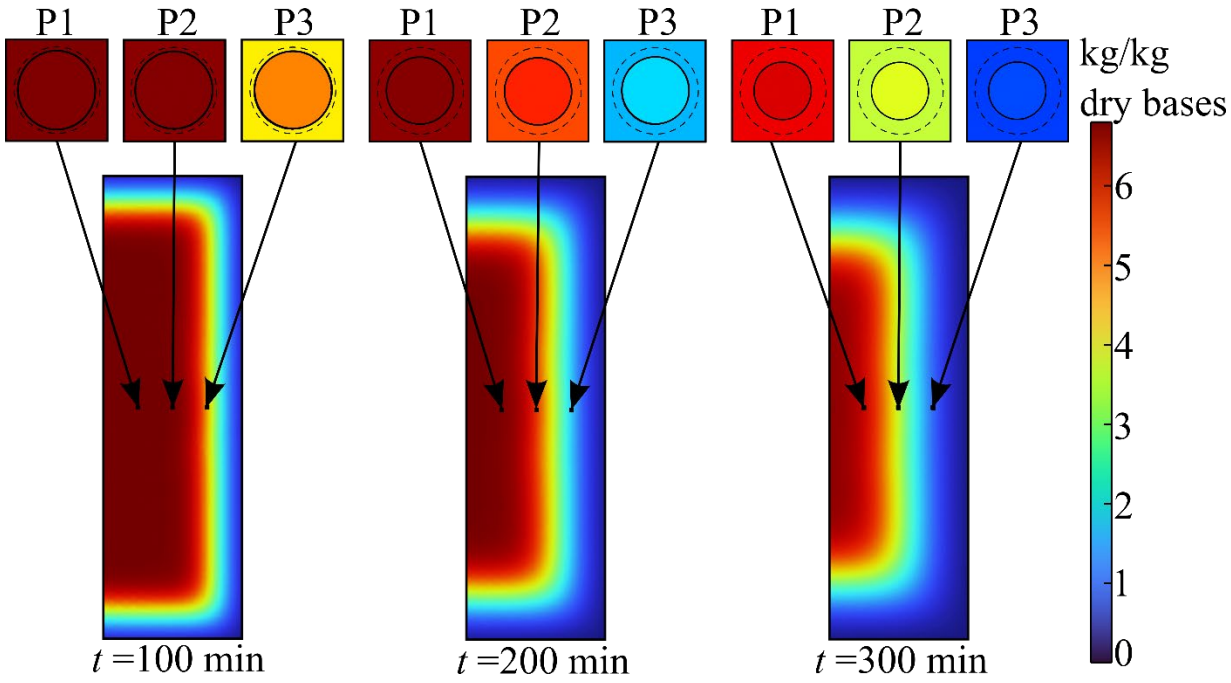

689

690 Figure 9. Multiscale moisture distribution (kg/kg dry bases) for drying at 47°C. Original cell

691 geometry visually represented by the dashed circle.

692

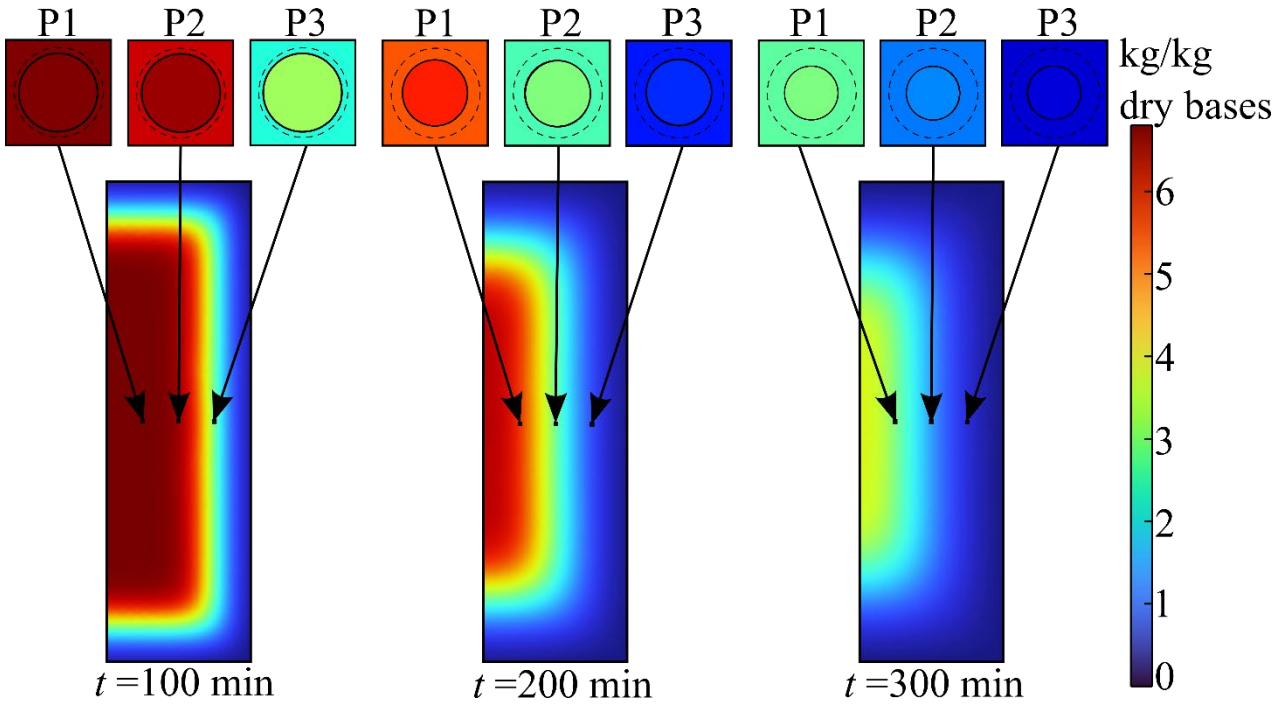

Figure 10. Multiscale moisture distribution (kg/kg dry bases) for drying at 64°C. Original cell geometry visually represented by the dashed circle.

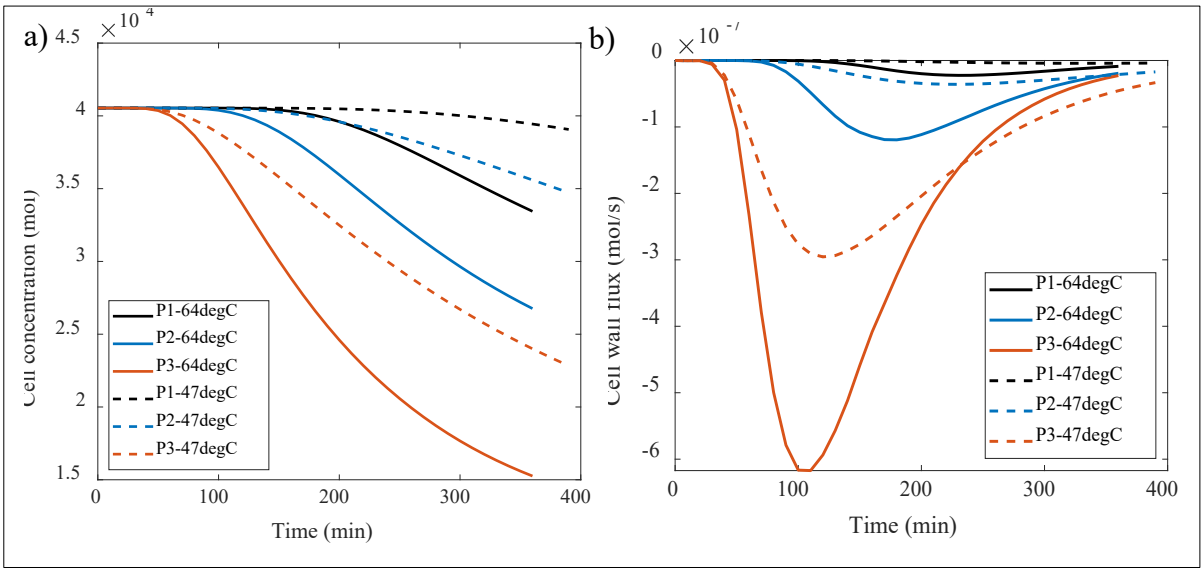

697

698 Figure 11. Intracellular water evolution for both drying temperatures, (a) concentration within
699 each intracellular space at the points of interest (mol), (b) Flux through the cell wall (mol/s) at
700 the points of interest.

701

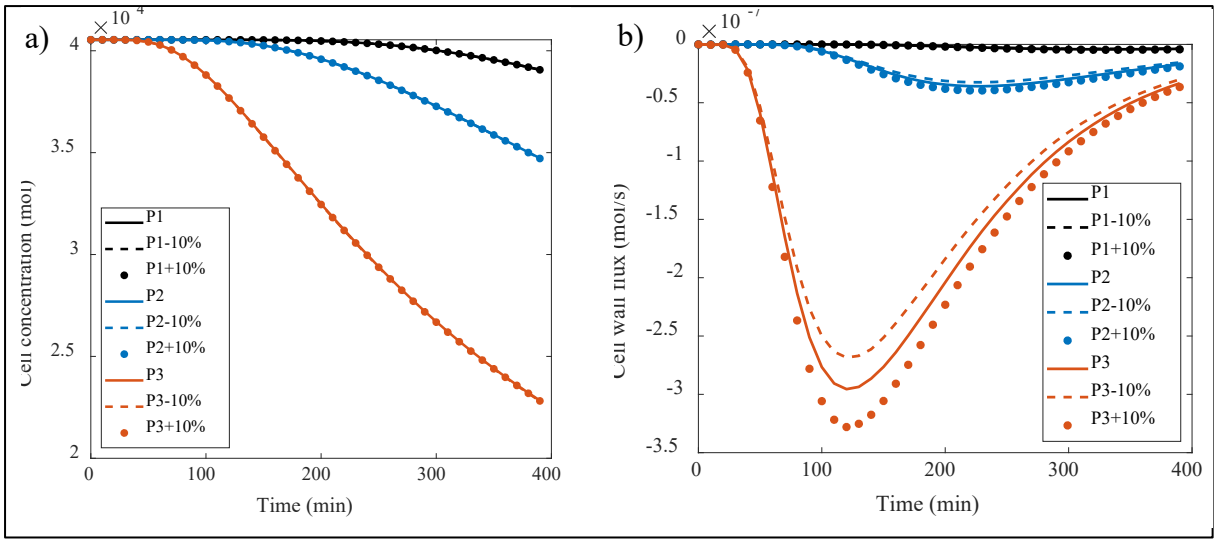

Figure 12. Sensitivity investigation for the cell wall permeability ±10%, a) moisture concentration (mol), at each point of interest b) cell wall flux (mol/s) at each point of interest.

706 **Tables:**

707 Table 1. Input parameters

Parameter	Value (unit)	Reference
Density of apple, ρ	837 (kg m^{-3})	Mavroudis et al. (1998)
Density of water, ρ_w	995 (kg m^{-3})	Cengel (2003)
Specific heat of apple, c_p	$1000(1.4+3.22M_{wb})$ (J kg^{-1} K^{-1})	Białobrzewski (2006)
Thermal conductivity of apple, k	$0.49-0.443\exp(-0.206M_{wb})$ (W/(m·K))	Mattea et al. (1986)
Initial moisture content, M_0	6.8 (kg kg^{-1} dry bases)	This study
Initial sample temperature, T_0	296 (K)	This study
Equilibrium moisture content, M_e	0.2 (kg kg^{-1} dry bases)	Białobrzewski (2006)
Initial wet basis moisture content, $M_{o_{wb}}$	0.86 (kg kg^{-1} wet bases)	This study
Latent heat of evaporation, h_{fg}	2358600 (J kg^{-1})	Cengel (2003)
Universal gas constant, R	8.314 (J mol^{-1} K^{-1})	Cengel and Boles (2002)
Molar mass of water, M_w	0.018016 (kg mol^{-1})	Cengel and Boles (2002)
Partial vapor pressure, $p_{v\,air}$	1250 (Pa)	(Welsh et al., 2023)
Heat transfer coefficient, h_T	13.2 (W m^{-2} K^{-1})	(Welsh et al., 2023)
Mass transfer coefficient, h_m	0.00381 (m s^{-1})	(Welsh et al., 2023)
Cell wall permeability	2 x 10^{-5} (m s^{-1})	(Ferrando & Spiess, 2001; Moshelion et al., 2004)

708